electronics

MDPI

Article

Low Power Consumption Gate-Tunable $WSe_2/SnSe_2$ van der Waals Tunnel Field-Effect Transistor

Abdelkader Abderrahmane, Changlim Woo and Pil-Ju Ko *

Department of Electrical Engineering, Chosun University, 375, Seosuk-dong, Dong-gu, Gwangju 501-759, Korea; abderrahmane.abdelkader@gmail.com (A.A.); 12ee34@chosun.kr (C.W.)
* Correspondence: pjko@chosun.ac.kr

Abstract: Two-dimensional (2D) transition-metal dichalcogenides (TMDCs) have attracted attention as promising next-generation electronic devices and sensors. In this study, we fabricated a novel nanoelectronic device based on a black-phosphorus-gated $WSe_2/SnSe_2$ van der Waals (vdW) tunnel field-effect transistor (TFET), where hexagonal boron nitride (h-BN) was used as the gate insulator. We performed morphological, electrical, and optoelectronic characterizations. The p-WSe_2/n-$SnSe_2$ heterostructure-based TFET exhibited *p*-type behavior with a good dependence on the gate voltage. The TFET device showed a trend toward negative differential resistance (NDR) originating from band-to-band tunneling, which can be tuned by applying a gate voltage. The optoelectronic performance of the TFET device was low, with a maximum photoresponsivity of 11 mA W^{-1}, owing to the large device length. The results obtained herein promote the integration of black phosphorus into low-energy-consumption 2D vdW TFETs.

Keywords: two-dimensional materials; transition-metal dichalcogenides; black phosphorus; hexagonal boron nitride; tungsten diselenide; tin diselenide; tunnel field-effect transistors

Citation: Abderrahmane, A.; Woo, C.; Ko, P.-J. Low Power Consumption Gate-Tunable $WSe_2/SnSe_2$ van der Waals Tunnel Field-Effect Transistor. *Electronics* **2022**, *11*, 833. https://doi.org/10.3390/electronics11050833

Academic Editor: Alina Caddemi

Received: 4 February 2022
Accepted: 4 March 2022
Published: 7 March 2022

1. Introduction

Two-dimensional (2D) van der Waals (vdW) heterostructures have been widely studied for the development of nanoelectronics. Transition-metal dichalcogenides (TMDCs) have attracted significant attention for several applications, such as memory and logic circuits [1,2], photocatalytic water splitting devices [3], field-effect transistors [4,5], tunneling transistors [6], bipolar junction transistors [7], ferroelectric field-effect transistor (FE) transistors [8,9], ferromagnetic transistors [10], and sensors [11–13]. Transition-metal dichalcogenides have suitable energy bandgaps for electronic and optoelectronic devices. In particular, tungsten diselenide (WSe_2), which is an intrinsic semiconductor [14] with an energy band gap of 1.2 eV for its bulk form (up to 1.65 eV for the monolayer) [15,16], and tin diselenide ($SnSe_2$), which is degenerately n-doped with an energy bandgap of 1.0 eV [17], are appropriate for such applications. Two-dimensional black phosphorus (BP) is promising for low-power-consumption electronic devices [18]. BP has an infrared band gap energy of ~0.3 eV (bulk), which is tunable to ~2 eV (monolayer) by reducing the layer thickness [19] and goes down to 0.05 eV by electric field modulation [20]. Hexagonal boron nitride (h-BN) is a dielectric material with a high band gap of ~6 eV, and thus, it is useful as an insulator layer for MOS devices and as a dielectric for device shielding [21].

In this study, we fabricated a novel low-power-consumption, gate-tunable $WSe_2/SnSe_2$ vdW tunnel field-effect transistor (TFET). We used BP as the gate contact and h-BN as the insulator layer between the gate and channel. We carried out morphological characterizations and investigated the electrical and optoelectronic properties of the gated $WSe_2/SnSe_2$ TFET, where the device showed a trend toward negative differential resistance (NDR) owing to the band-to-band tunneling (BTBT) phenomenon. We were able to control the tunneling effect by varying the applied gate voltage.

2. Materials and Methods

BP, hexagonal boron nitride (h-BN), tungsten diselenide (WSe_2), and tin diselenide ($SnSe_2$) were purchased from HQ Graphene; X-ray Diffraction (XRD) data of the 2D materials are shown in Figure S1. The fabrication process is shown schematically in Figure 1. First, chromium/gold (10/50 nm) were deposited by thermal evaporation onto a 300-nm SiO_2/silicon substrate, followed by the successive deposition of few-layered BP (gate contact) and h-BN (gate insulator) through the mechanical exfoliation technique using flexible polydimethylsiloxane (PDMS). Subsequently, few-layered n-type $SnSe_2$ and *p*-type WSe_2 were successively deposited using the same technique. The device was not annealed to prevent $SnSe_2$ degradation. The morphological properties were observed using scanning electron microscopy (SEM; Hitachi TM-1000; Japan) and atomic force microscopy (AFM; inVia Reflex). For electrical and optoelectronic characterizations, we used a HP 4155A semiconductor parameter analyzer. Optoelectronic properties were evaluated using a laser source with power values varying from 0.015 to 3.193 μW, wavelength, and spot diameter of 532 and 20 μm, respectively.

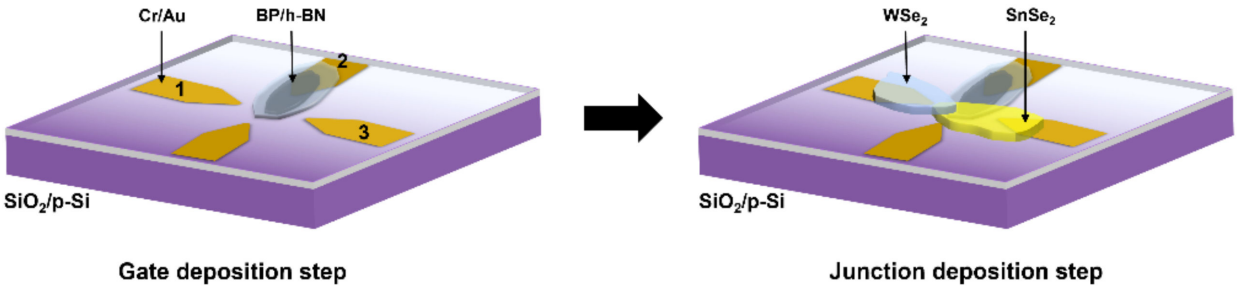

Figure 1. Schematic representation of the fabricated $WSe_2/SnSe_2$ van der Waals heterostructure-based gated tunnel field-effect transistor.

3. Results and Discussion

3.1. Morphological Characterization

Figure 2a shows an SEM image of the gated TFET, showing multilayered WSe_2, $SnSe_2$, and h-BN/BP in blue, yellow, and white dotted lines, respectively. The length of the device was 30 μm. The h-BN/BP junction and WSe_2 did not intersect in the vertical direction, as observed in the figure; thus, the thickness of the insulator was roughly estimated to be 2 μm based on the distance between the edges of multilayered BP and WSe_2 (white arrows in Figure 3a). Figure 2b shows the corresponding AFM image, where the red, blue, pink, and purple lines indicate the cross-sections of the WSe_2, $SnSe_2$, h-BN, and h-BN/BP junctions, respectively. The thicknesses of the top WSe_2, $SnSe_2$, h-BN, and h-BN/BP junctions were determined by topographic analysis at 36, 76, 20, and 70 nm, respectively, as shown in Figure 2c. Thus, the thickness of multilayered BP was determined to be 50 nm.

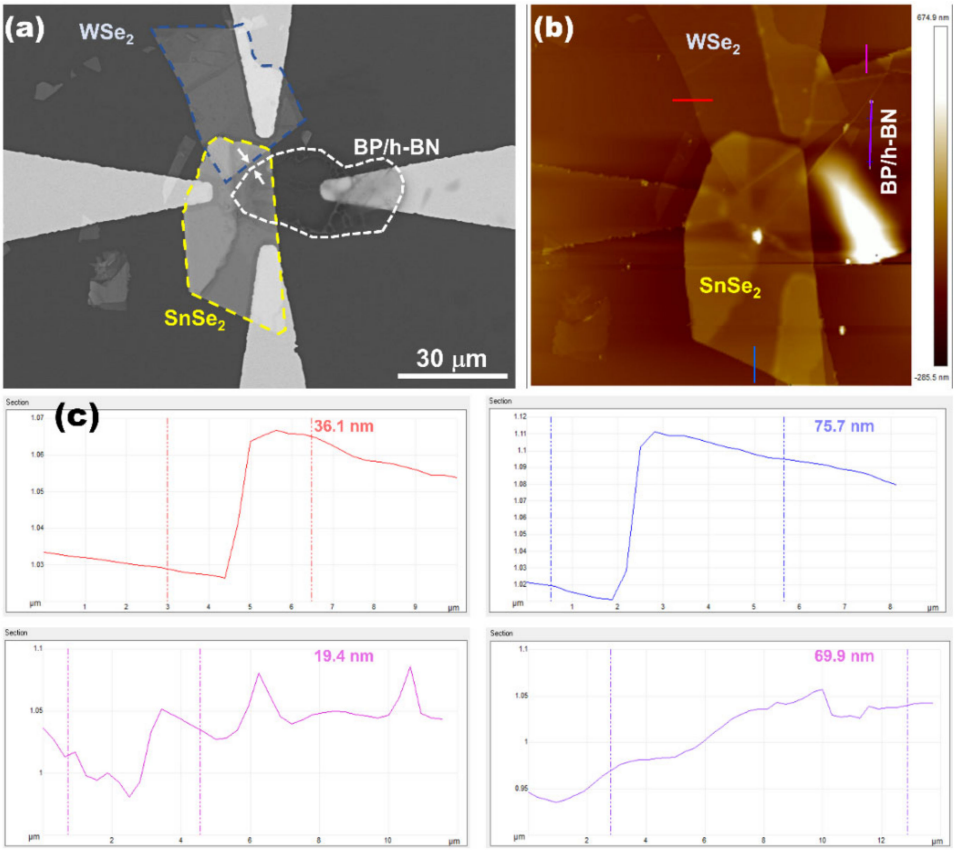

Figure 2. (**a**) SEM image and (**b**) AFM image of the BP-gated $WSe_2/SnSe_2$ van der Waals heterostructure. (**c**) Corresponding topographic analysis of WSe_2, $SnSe_2$, h-BN, and h-BN/BP junction.

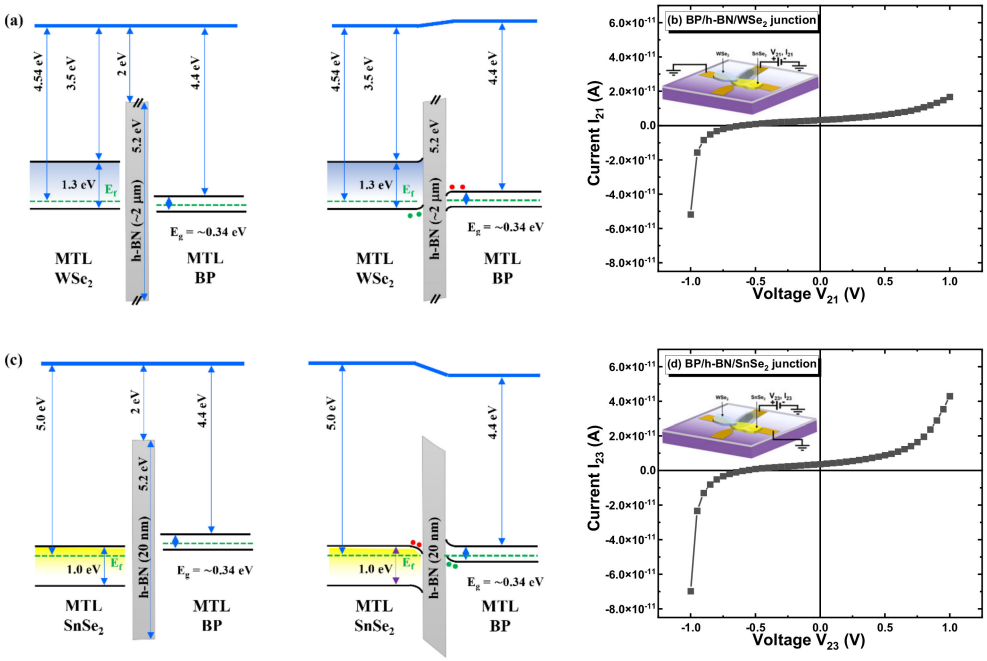

Figure 3. Energy band diagram of (**a**) p-WSe_2/h-BN/BP and (**c**) n-$SnSe_2$/h-BN/BP vdW heterostructures. I–V curves in vertical directions for (**b**) p-WSe_2/h-BN/BP and (**d**) n-$SnSe_2$/h-BN/BP vdW heterostructures.

3.2. Energy Band Diagram

Figure 3a,c shows the energy band diagrams of the device in the vertical direction, i.e., Figure 3a,c corresponds to the p-WSe_2/h-BN/BP and n-$SnSe_2$/h-BN/BP heterostructures, respectively. The energy band gap for $SnSe_2$ is ~1.0 eV, its electron affinity is 4.85 eV, and its work function is 5.0 eV [22]. For WSe_2, the energy band gap and electron affinity are 1.3 and 3.5 eV, respectively [23]. In both configurations, the heterostructures are in accumulation mode: accumulation of holes and electrons at the p-WSe_2/h-BN and the n-$SnSe_2$/h-BN interface, respectively. Figure 3b,d shows the corresponding current–voltage (I–V) curves. When the absolute value of the voltage was increased to 1 V, the current increased, which was probably due to the tunneling effect in the vertical direction because the insulator layer was very thin (20 nm).

3.3. Electrical and Optoelectronic Characterizations

Figure 4a,b shows the transfer characteristics of the BP-gated *p*-WSe_2/n-$SnSe_2$ heterostructure when $SnSe_2$ and WSe_2 were used, respectively. Both configurations exhibited *p*-type behavior, where the current increased with decreasing gate voltage. When grounding multilayered WSe_2, the device demonstrated good gate voltage dependence in both cases with an I_{ON}/I_{OFF} ratio of 20 at a polarization voltage of 2 V (Figure 4b).

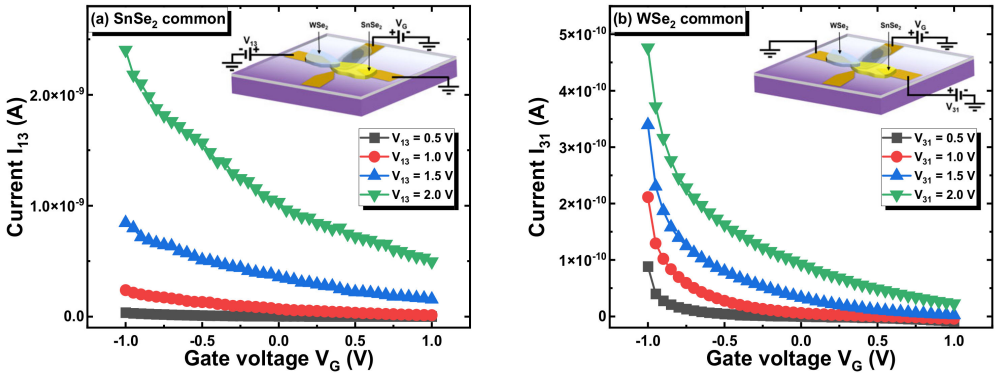

Figure 4. Gate voltage dependence of the current in BP-gated p-WSe_2/n-$SnSe_2$ heterostructure with (**a**) common $SnSe_2$ and (**b**) common Wse_2.

To investigate the current transport in the BP-gated *p*-Wse_2/n-$SnSe_2$ heterostructure, we drew an energy band diagram in the longitudinal direction, as shown in Figure 5a. At equilibrium, the *p*-Wse_2/n-$SnSe_2$ heterostructure showed a broken (type-III) band alignment. Figure 5b,c shows the I–V characteristics of the p-Wse_2/n-$SnSe_2$ heterostructure when $SnSe_2$ and Wse_2, respectively, were used as common contacts at different gate voltages. The gate voltage had a lower effect when Wse_2 was used as a common contact because BP and Wse_2 had no intersection, as shown in Figure 2. As shown in Figure 5b, a change in the current curve was observed around a polarization and gate voltage of 1 V. Similar behavior was observed in a *p*-Si back-gated Wse_2/$SnSe_2$ heterostructure, which was explained by the trend toward NDR [24]. When the gate voltage was decreased from 1 to −1 V, the I–V curves shifted to lower voltages.

Figure 6a shows the log-scale current at different gate voltages. Two distinct linear regimes can be observed in the forward current region. The two observed regimes can be modeled using direct tunneling (DT) and Fowler–Nordheim tunneling (FNT), according to the following equations [25]:

$$I_{DT}(V) = \frac{Aq^2 V_{ds}\sqrt{m\varphi_B}}{h^2 d} exp\left[\frac{-4\pi d\sqrt{m^*\varphi_B}}{h}\right] \quad (1)$$

$$I_{FNT}(V) = \frac{Aq^3 m {V_{ds}}^2}{8\pi h\varphi_B d^2 m^*} exp\left[\frac{-8\pi d{\varphi_B}^{3/2}\sqrt{2m^*}}{3hqV_{ds}}\right] \quad (2)$$

where A, φ_B, q, m, m^*, d, and h are the effective contact area, barrier height, electron charge, free-electron mass, effective electron mass, barrier width, and Planck's constant, respectively. Ln (I/V^2) versus $1/V$ is plotted in Figure 6b; according to Equations (1) and (2), the curve should show linear and logarithmic regimes for FNT and DT, respectively. From the same figure, DT occurs at a low voltage and FNT dominates at a high voltage with a linear negative slope.

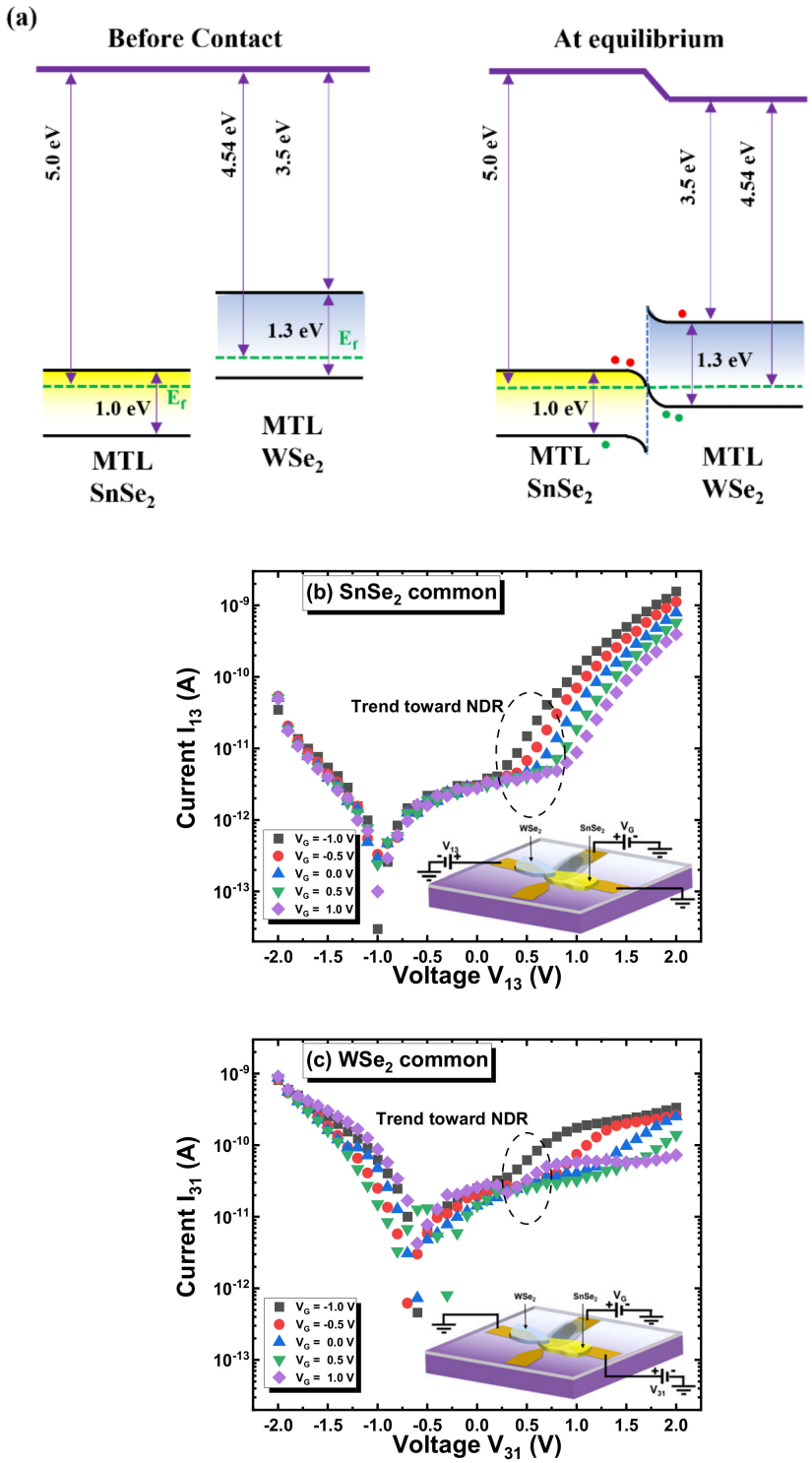

Figure 5. (**a**) Energy band diagram of p-WSe_2/ n-$SnSe_2$ heterostructure in the longitudinal direction. I–V curves in longitudinal directions when (**b**) $SnSe_2$ and (**c**) Wse_2 are used as common contact.

DT occurred at a low voltage in the positive gate voltage and forward regime (Figure 6c). However, when the polarization voltage increases to higher values, a change from broken (type-III) to staggered (type-II) can occur. Therefore, the BTBT phenomenon is weakened, and Fowler–Nordheim tunneling dominates. The inverse polarization (Figure 6d) revealed a diode-like band structure with electron and hole energy barriers at the *p*-Wse_2/n-$SnSe_2$ interface, which is the origin of the low reverse current. When a negative gate voltage was applied between BP and $SnSe_2$, the valence and conduction bands of $SnSe_2$ increased, and the BTBT phenomenon was weakened at a low polarization voltage. However, at higher polarization voltage values (Figure 6e), the FNT current was enhanced, which can explain the current shift to higher values observed in Figure 5b when a negative gate voltage was applied. Figure 6f shows the I–V curves of the positively polarized p-Wse_2/n-$SnSe_2$ heterostructure in dark and under a light excitation of 0.015 μW; the light enhanced the current and caused a shift to higher voltage values owing to the enhancement of the DT current.

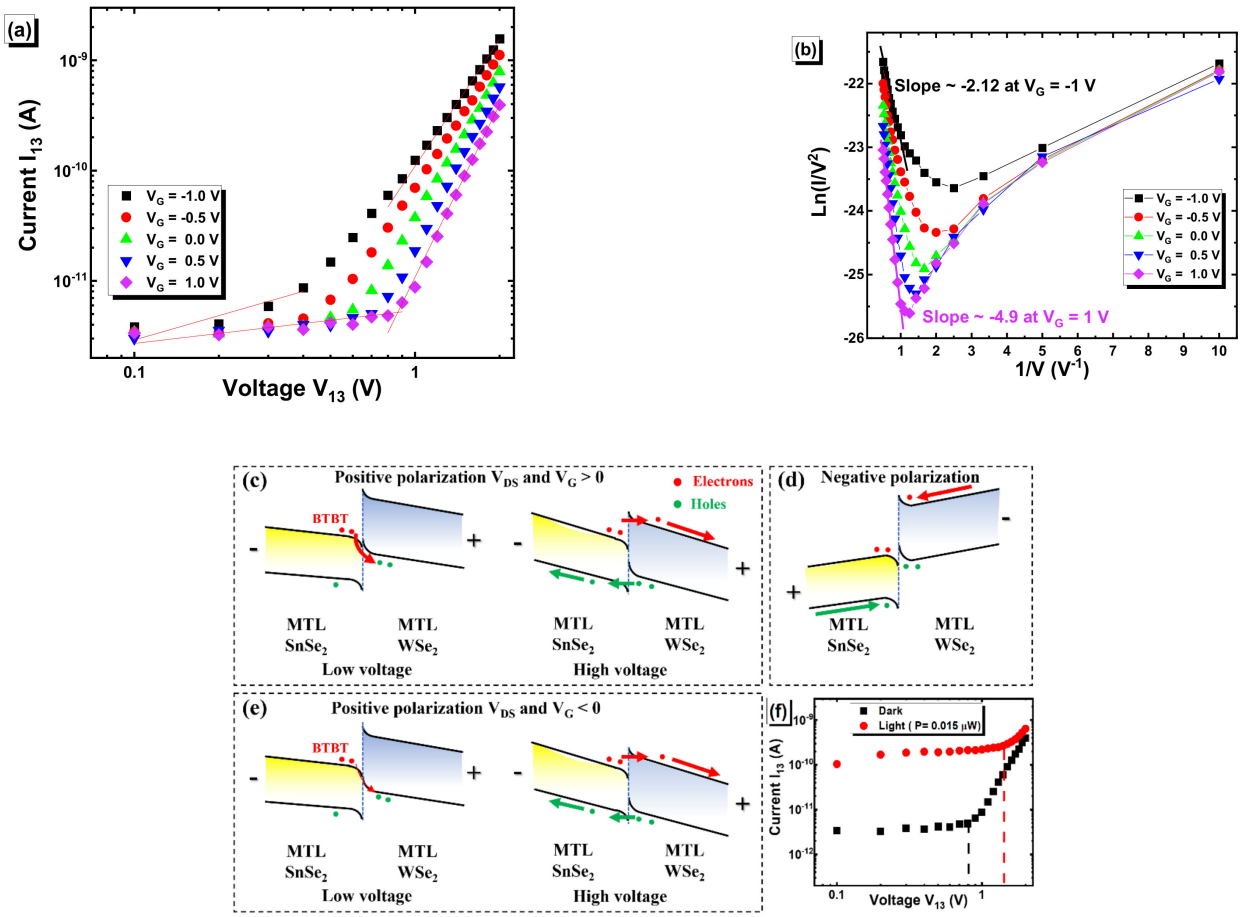

Figure 6. (**a**) Log current scale in the forward region and its corresponding (**b**) ln (I/V^2)–1/V curve, energy band diagrams of p-WSe_2/n-$SnSe_2$ heterostructure, (**c**) ($V_{DS} > 0$ and $V_G > 0$), (**d**) ($V_{DS} < 0$ and $V_G > 0$), (**e**) ($V_{DS} > 0$ and $V_G < 0$), and (**f**) I–V curves of p-WSe_2/n-$SnSe_2$ heterostructure in dark and under light excitation.

Finally, the optoelectronic properties of the heterostructures were investigated. Figure 7a–d shows the I–V characteristics at different values of the gate voltage and laser power. When the laser power was increased, the current increased because of photogenerated carriers (electrons in the conduction bands and holes in the valence bands).

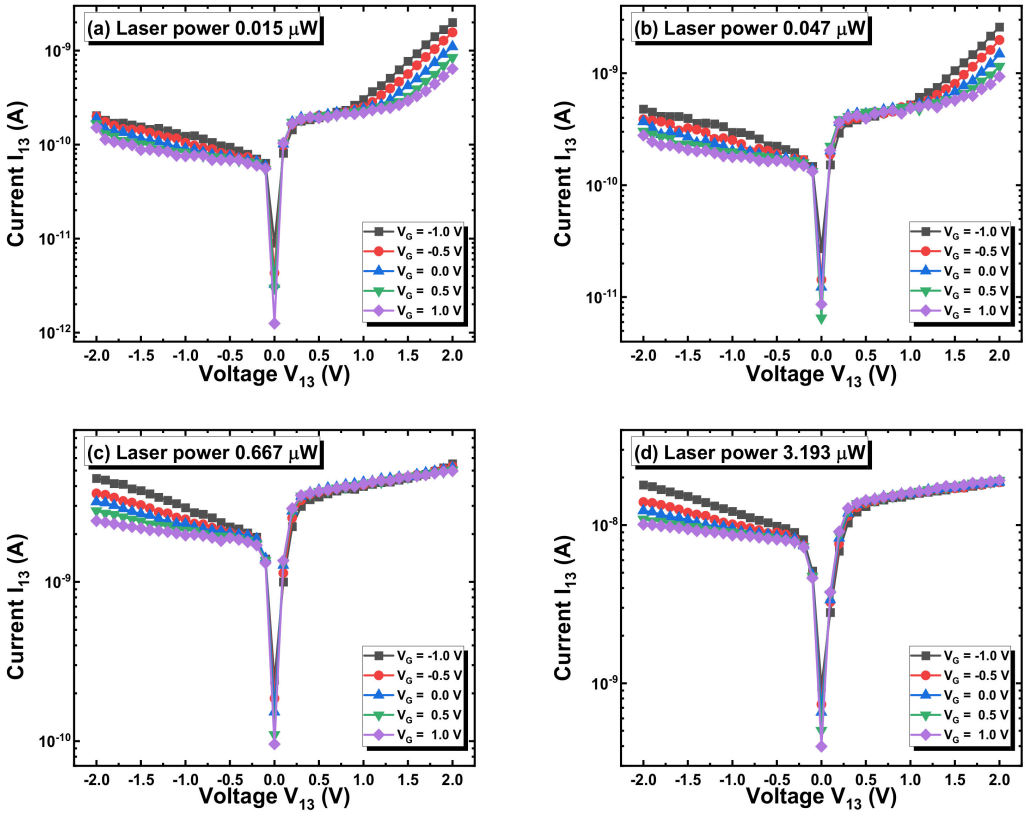

Figure 7. I–V curves in the longitudinal direction when $SnSe_2$ was used as the common contact at different values of gate voltage and at a laser power value of (**a**) 0.015, (**b**) 0.047, (**c**) 0.667, and (**d**) 3.193 μW.

The photoresponsivity was deduced according to the equation $R_\lambda = |I_{ph}|/P = |I_{light} - I_{dark}|/P$, where I_{ph} represents the photocurrent and P is the laser power. Figure 8a,b corresponds to the photoresponsivity of the p-WSe_2/n-$SnSe_2$ heterostructure-based TFET at negative and positive polarization voltages, respectively. The variation in the photoresponsivity was more homogeneous at a polarization voltage of −2 V (Figure 8a) and it increased to ~11 mA W^{-1} at a gate voltage of −1 V and laser power of 0.015 μW. Moreover, it decreased when the laser power is increased, a phenomenon that is commonly observed in TMDC-based photodetectors [26], which is attributed to the trapping effect.

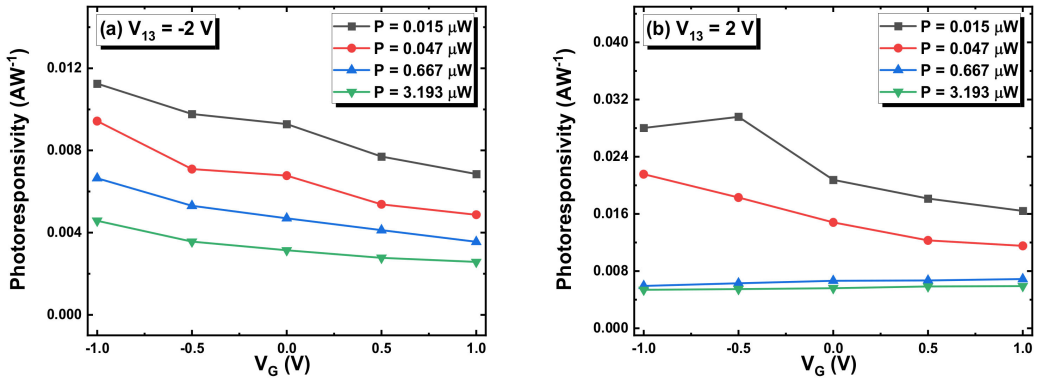

Figure 8. Gate voltage and laser power dependence of the photoresponsivity in p-WSe_2/n-$SnSe_2$ heterostructure-based TFET at (**a**) negative and (**b**) positive polarization voltages.

The optoelectronic properties of WSe_2/$SnSe_2$ heterojunctions have not been investigated in detail. As seen in Table 1, the photoresponsivity of our device was larger than the value reported by Chauhan et al. [27] but lower than those reported by Xue et al. [28]

and Sun et al. [29]. The low photoresponsivity was due to the long channel length of the device (30 μm). It should be noted that both the photoresponsivity and I_{ON}/I_{OFF} ratio can be improved using multiple interdigitated electrodes and by shortening the channel length.

Table 1. Comparison of figures-of-merit for photodetectors based on WSe_2/ $SnSe_2$ heterojunction.

Structure	Spectral Range	R_λ (mAW^{-1})	I_{ON}/I_{OFF} Ratio	Reference
BP-gated $WSe_2/SnSe_2$	532 nm	11	20	This work
$WSe_2/SnSe_2$	532 nm	1.03	N/A	[27]
$WSe_2/SnSe_2$	532 nm	N/A	10^6	[24]
$WSe_2/SnSe_2$	532 nm	588×10^3	~10^4	[28]
$WSe_2/SnSe_2$	700 nm	450	~10^3 to ~10^4	[29]

4. Conclusions

We fabricated a BP-gated $WSe_2/SnSe_2$ vdW TFET. We carried out morphological characterizations and investigated the electrical and optoelectronic properties of the *p*-WSe_2/n-$SnSe_2$ heterostructure in the vertical and longitudinal directions. The TFET device showed *p*-type behavior with good dependence on the gate voltage and a trend toward NDR originating from BTBT phenomenon. We succeeded in controlling the tunneling effect by varying the applied gate voltage. The maximum photoresponsivity of the device was ~11 mA W^{-1}, which was slightly small because of the long channel length of our device (30 μm). We believe that the results presented herein will promote the fabrication of tunneling effect transistors based only on two-dimensional materials. In future research, we believe that the optimization of the device dimensions will significantly improve its electrical and optoelectronic performance.

Supplementary Materials: The following supporting information can be downloaded at: https://www.mdpi.com/article/10.3390/electronics11050833/s1, Figure S1: X-ray diffraction (XRD) images of black phosphorus (BP), hexagonal boron nitride (h-BN), tungsten diselenide (WSe2), and tin diselenide (SnSe2).

Author Contributions: Methodology, C.W.; writing—original draft preparation, A.A.; writing—review and editing, P.-J.K. All authors have read and agreed to the published version of the manuscript.

Funding: This work was supported by the Brain Pool Program through the National Research Foundation of Korea (NRF), funded by the Ministry of Science and ICT (NRF-2019H1D3A1A01102658). This study was supported by a research fund from Chosun University, 2021.

Data Availability Statement: Data is available from the corresponding author upon the request.

Conflicts of Interest: The authors declare no conflict of interest.

References

1. Tong, L.; Peng, Z.; Lin, R.; Li, Z.; Wang, Y.; Huang, X.; Xue, K.-H.; Xu, H.; Liu, F.; Xia, H.; et al. 2D materials–based homogeneous transistor-memory architecture for neuromorphic hardware. *Science* **2021**, *373*, 1353–1358. [CrossRef] [PubMed]
2. Yin, L.; Cheng, R.; Wang, Z.; Wang, F.; Sendeku, M.G.; Wen, Y.; Zhan, X.; He, J. Two-Dimensional Unipolar Memristors with Logic and Memory Functions. *Nano Lett.* **2020**, *20*, 4144–4152. [CrossRef]
3. Shanker, G.S.; Biswas, A.; Ogale, S.B. 2D materials and their heterostructures for photocatalytic water splitting and conversion of CO_2 to value chemicals and fuels. *J. Phys. Energy* **2021**, *3*, 022003. [CrossRef]
4. Conti, S.; Pimpolari, L.; Calabrese, G.; Worsley, R.; Majee, S.; Polyushkin, D.K.; Paur, M.; Pace, S.; Keum, D.H.; Fabbri, F.; et al. Low-voltage 2D materials-based printed field-effect transistors for integrated digital and analog electronics on paper. *Nat. Commun.* **2020**, *11*, 3566. [CrossRef] [PubMed]
5. Abderrahmane, A.; Ko, P.J.; Thu, T.V.; Ishizawa, S.; Takamura, T.; Sandhu, A. High photosensitivity few-layered $MoSe_2$ back-gated field-effect phototransistors. *Nanotechnology* **2014**, *25*, 365202. [CrossRef] [PubMed]
6. Das, S.; Prakash, A.; Salazar, R.; Appenzeller, J. Toward low-power electronics: Tunneling phenomena in transition metal dichalcogenides. *ACS Nano* **2014**, *8*, 1681–1689. [CrossRef]
7. Zhu, W.; Low, T.; Wang, H.; Ye, P.; Duan, X. Nanoscale electronic devices based on transition metal dichalcogenides. *2D Mater.* **2019**, *6*, 032004. [CrossRef]

8. Luo, Z.-D.; Xia, X.; Yang, M.-M.; Wilson, N.R.; Gruverman, A.; Alexe, M. Artificial optoelectronic synapses based on ferroelectric field-effect enabled 2D transition metal dichalcogenide memristive transistors. *ACS Nano* **2019**, *14*, 746–754. [CrossRef]
9. Kim, J.Y.; Choi, M.-J.; Jang, H.W. Ferroelectric field effect transistors: Progress and perspective. *APL Mater.* **2021**, *9*, 021102. [CrossRef]
10. Xie, L.; Cui, X. Manipulating spin-polarized photocurrents in 2D transition metal dichalcogenides. *Proc. Natl. Acad. Sci. USA* **2016**, *113*, 3746–3750. [CrossRef]
11. Wang, L.; Xu, D.; Jiang, L.; Gao, J.; Tang, Z.; Xu, Y.; Chen, X.; Zhang, H. Transition Metal Dichalcogenides for Sensing and Oncotherapy: Status, Challenges, and Perspective. *Adv. Funct. Mater.* **2021**, *31*, 2004408. [CrossRef]
12. Urbanos, F.J.; Gullace, S.; Samorì, P. Field-Effect Transistors Based Ion Sensors: Ultrasensitive Mercury (II) Detection via Healing of MoS2 Defects. *Nanoscale* **2021**, *13*, 19682–19689. [CrossRef] [PubMed]
13. Shu, Y.; Yang, Y.; Gao, Q. Interlayer engineering of two-dimensional transition-metal disulfides for electrochemical and optical sensing applications. *FlatChem* **2021**, *27*, 100242. [CrossRef]
14. Jin, Z.; Li, X.; Mullen, J.T.; Kim, K.W. Intrinsic transport properties of electrons and holes in monolayer transition-metal dichalcogenides. *Phys. Rev. B* **2014**, *90*, 045422. [CrossRef]
15. Yu, P.; Lin, J.; Sun, L.; Le, Q.L.; Yu, X.; Gao, G.; Hsu, C.-H.; Wu, D.; Chang, T.-R.; Zeng, Q.; et al. Metal-Semiconductor Phase-Transition in $WSe_{2(1-x)}$ Te_{2x} Monolayer. *Adv. Mater.* **2017**, *29*, 1603991. [CrossRef] [PubMed]
16. Choi, W.; Choudhary, N.; Han, G.H.; Park, J.; Akinwande, D.; Lee, Y.H. Recent development of two-dimensional transition metal dichalcogenides and their applications. *Mater. Today* **2017**, *20*, 116–130. [CrossRef]
17. Narro-Rios, J.S.; Ramachandran, M.; Martínez-Escobar, D.; Sánchez-Juárez, A. Ultrasonic spray pyrolysis deposition of SnSe and SnSe2 using a single spray solution. *J. Semicond.* **2013**, *34*, 013001. [CrossRef]
18. Abderrahmane, A.; Woo, C.; Ko, P.J. Black Phosphorus/Molybdenum Diselenide Heterojunction-Based Photodetector. *J. Electron. Mater.* **2021**, *50*, 5713–5720. [CrossRef]
19. Li, J.; Luo, H.; Zhai, B.; Lu, R.; Guo, Z.; Zhang, H.; Liu, Y. Black phosphorus: A two-dimension saturable absorption material for mid-infrared Q-switched and mode-locked fiber lasers. *Sci. Rep.* **2016**, *6*, 30361. [CrossRef]
20. Zong, X.; Hu, H.; Ouyang, G.; Wang, J.; Shi, R.; Zhang, L.; Zeng, Q.; Zhu, C.; Chen, S.; Cheng, C.; et al. Black phosphorus-based van der Waals heterostructures for mid-infrared light-emission applications. *Light Sci. Appl.* **2020**, *9*, 114. [CrossRef]
21. Li, A.; Chen, Q.; Wang, P.; Gan, Y.; Qi, T.; Wang, P.; Tang, F.; Wu, J.Z.; Chen, R.; Zhang, L.; et al. Ultrahigh-sensitive broadband photodetectors based on dielectric shielded $MoTe_2$/Graphene/SnS_2 p–g–n junctions. *Adv. Mater.* **2019**, *31*, e1805656. [CrossRef] [PubMed]
22. Mukhokosi, E.P.; Roul, B.; Krupanidhi, S.B.; Nanda, K.K. Toward a fast and highly responsive SnSe2-based photodiode by exploiting the mobility of the counter semiconductor. *ACS Appl. Mater. Interfaces* **2019**, *11*, 6184–6194. [CrossRef] [PubMed]
23. Schulman, D.S.; Arnold, A.J.; Das, S. Contact engineering for 2D materials and devices. *Chem. Soc. Rev.* **2018**, *47*, 3037–3058. [CrossRef] [PubMed]
24. Yan, X.; Liu, C.; Li, C.; Bao, W.; Ding, S.; Zhang, D.W.; Zhou, P. Tunable SnSe2/WSe2 heterostructure tunneling field effect transistor. *Small* **2017**, *13*, 1701478. [CrossRef]
25. Vu, Q.A.; Lee, J.H.; Nguyen, V.L.; Shin, Y.S.; Lim, S.C.; Lee, K.; Heo, J.; Park, S.; Kim, K.; Lee, Y.H.; et al. Tuning carrier tunneling in van der Waals heterostructures for ultrahigh detectivity. *Nano Lett.* **2017**, *17*, 453–459. [CrossRef]
26. Furchi, M.M.; Polyushkin, D.; Pospischil, A.; Mueller, T. Mechanisms of photoconductivity in atomically thin MoS_2. *Nano Lett.* **2014**, *14*, 6165–6170. [CrossRef]
27. Chauhan, P.; Patel, A.B.; Solanki, G.K.; Machhi, H.K.; Sumesh, C.K.; Soni, S.S.; Patel, V.; Pathak, V.M. Ultrasonically exfoliated nanocrystal-based Z-scheme SnSe2/WSe2 heterojunction for a superior electrochemical photoresponse. *J. Phys. Chem. C* **2021**, *125*, 14729–14740. [CrossRef]
28. Xue, H.; Dai, Y.; Kim, W.; Wang, Y.; Bai, X.; Qi, M.; Halonen, K.; Lipsanen, H.; Sun, Z. High photoresponsivity and broadband photodetection with a band-engineered WSe 2/SnSe 2 heterostructure. *Nanoscale* **2019**, *11*, 3240–3247. [CrossRef]
29. Sun, Y.; Hu, R.; An, C.; Ma, X.; Zhang, J.; Liu, J. Visible to near-infrared photodetector based on SnSe2/WSe2 heterojunction with potential application in artificial visual neuron. *Nanotechnology* **2021**, *32*, 475206. [CrossRef]